

## Article

# Genesis of Coalbed Methane and Its Storage and Seepage Space in Baode Block, Eastern Ordos Basin

Hao Chen <sup>1</sup>, Wenguang Tian <sup>1,\*</sup>, Zhenhong Chen <sup>1</sup>, Qingfeng Zhang <sup>2</sup> and Shu Tao <sup>3,\*</sup>

<sup>1</sup> PetroChina Research Institute of Petroleum Exploration and Development, Beijing 100083, China; chen hao69@petrochina.com.cn (H.C.); Chenzhenhong@petrochina.com.cn (Z.C.)

<sup>2</sup> PetroChina Coalbed Methane Company Limited, Beijing 100028, China; zqf2012@petrochina.com.cn

<sup>3</sup> School of Energy Resources, China University of Geosciences, Beijing 100083, China

\* Correspondence: tianwg69@petrochina.com.cn (W.T.); peach888@163.com (S.T.)

**Abstract:** The Baode block on the eastern margin of the Ordos Basin is a key area for the development of low-rank coalbed methane (CBM) in China. In order to find out the genesis of CBM and its storage and seepage space in Baode block, the isotopic testing of gas samples was carried out to reveal the origin of CH<sub>4</sub> and CO<sub>2</sub>, as well, mercury intrusion porosimetry, low temperature nitrogen adsorption, and X-ray CT tests were performed to characterize the pores and fractures in No. 4 + 5 and No. 8 + 9 coal seams. The results showed that the average volume fraction of CH<sub>4</sub>, N<sub>2</sub>, and CO<sub>2</sub> is 88.31%, 4.73%, and 6.36%, respectively. No. 4 + 5 and No. 8 + 9 coal seams both have biogenic gas and thermogenic methane. Meanwhile, No. 4 + 5 and No. 8 + 9 coal seams both contain CO<sub>2</sub> generated by coal pyrolysis, which belongs to organic genetic gas, while shallow CO<sub>2</sub> is greatly affected by the action of microorganisms and belongs to biogenic gas. The average proportion of micropores, transition pores, mesopores, and macropores is 56.61%, 28.22%, 5.10%, and 10.07%, respectively. Samples collected from No. 4 + 5 coal seams have developed more sorption pores. Meanwhile, samples collected from No. 8 + 9 coal seams exhibited a relatively low degree of hysteresis (Hg retention), suggesting good pore connectivity and relatively high seepage ability, which is conducive to gas migration. The connected porosity of coal samples varies greatly, mainly depending on the relative mineral content and the proportion of connected pores.

**Keywords:** genesis of coalbed methane; pore-fracture system; storage and seepage space; Baode block



**Citation:** Chen, H.; Tian, W.; Chen, Z.; Zhang, Q.; Tao, S. Genesis of Coalbed Methane and Its Storage and Seepage Space in Baode Block, Eastern Ordos Basin. *Energies* **2022**, *15*, 81. <https://doi.org/10.3390/en15010081>

Academic Editors:

Nikolaos Koukouzas and  
Reza Rezaee

Received: 23 October 2021

Accepted: 21 December 2021

Published: 23 December 2021

**Publisher's Note:** MDPI stays neutral with regard to jurisdictional claims in published maps and institutional affiliations.



**Copyright:** © 2021 by the authors. Licensee MDPI, Basel, Switzerland. This article is an open access article distributed under the terms and conditions of the Creative Commons Attribution (CC BY) license (<https://creativecommons.org/licenses/by/4.0/>).

## 1. Introduction

Following the Qinshui Basin, the Ordos Basin is another large gas field in China with proven reserves of more than 100 billion cubic meters. It is also the first demonstration area for the exploration and development of low- and medium-rank coalbed methane (CBM) in China [1,2]. The Carboniferous Permian coal seams in the Ordos Basin have undergone different degrees of subsidence, uplift, and denudation, resulting in different degrees of thermal evolution of coal seams in different regions [3–5]. The Baode block is located in the northern part of the eastern margin of the Ordos Basin. The  $R_{o,max}$  of coal ranges from 0.52% to 0.89%, belonging to low- and middle-rank bituminous coal. Some CBM wells in the Baode block have obtained industrial gas flow, showing a good prospect for CBM development [6,7].

Previous studies have made preliminary discussions on the formation conditions and genetic types of CBM in the eastern margin of the Ordos Basin, and pointed out that the shallow part is a mixture of secondary biogas and thermogenic gas, while the deep part is mainly composed of thermogenic gas [8,9]. However, there is a lack of a systematic understanding of the origin of CBM in Baode block. In addition to methane, low-rank coal reservoirs often contain a certain proportion of CO<sub>2</sub> and N<sub>2</sub>, which can be used as important objects for studying the genesis of CBM [10].

In the current study, based on proximate analysis, mean vitrinite reflectance ( $R_o$ ) measurements and maceral analyses, the material composition (including macerals, ash,

moisture, volatile) of nine coal samples collected from Baode block were characterized. At the same time, isotopic testing of 54 gas samples collected from desorption tanks in different desorption periods was carried out to reveal the gas composition characteristics and gas genesis. Finally, based on high-pressure mercury injection, low-temperature liquid nitrogen, and X-ray CT experiments, the gas storage and seepage space were finely characterized, which provides a theoretical basis for further clarifying the direction of CBM exploration and development in the Baode block.

## 2. Geologic Setting

The Ordos Basin, a huge intra-cratonic basin, is located in North China and contains the second largest accumulation of coal resources in China [11,12] (Figure 1a). The basin is divided into seven structural units [13,14] (Figure 1b). The eastern margin of the Ordos Basin is a N–S striking and west-inclined monocline within the following three tectonic units: Weibei uplift in the north, Yimeng uplift in the south, and Jinxi fold in the middle [15–17] (Figure 1b). The Baode block is located in the northern part of the eastern margin of the Ordos Basin (Figure 1c). The formation is gentle, sloping westward at an angle of  $1^{\circ}$  to  $5^{\circ}$ . The faults are rare and small in scale, and the faults are mainly in the northeast direction with a fault distance of 10–25 m.

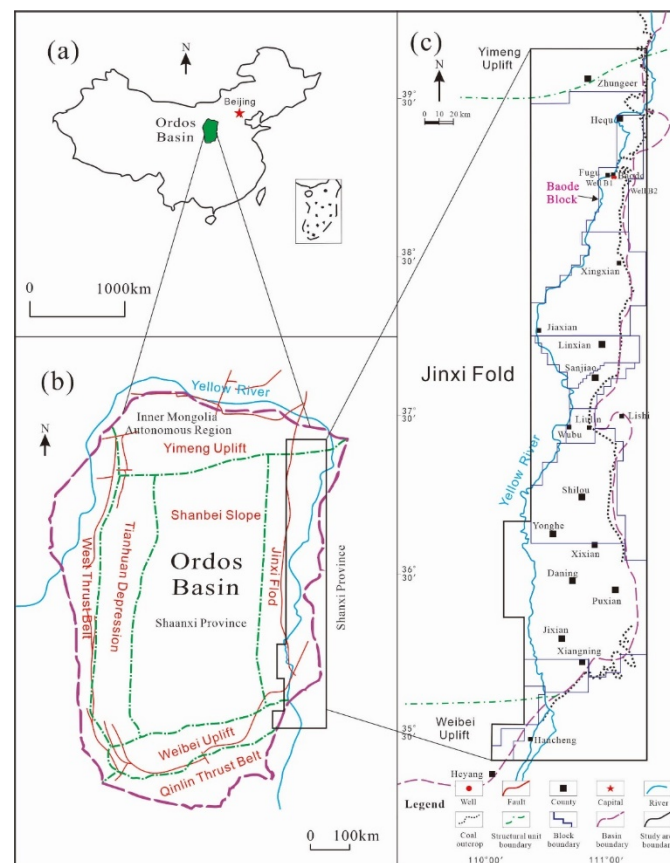


**Figure 1.** (a) Location of the Ordos Basin. (b) Tectonic units of the Ordos Basin. (c) Division of eastern margin of Ordos Basin and the location of Baode block, with the location of Wells B1 and B2.

In the Baode block, the main coal-bearing sequences occur in the Upper Carboniferous Taiyuan Formation ( $C_3t$ ) and the Lower Permian Shanxi Formation ( $P_1s$ ) (Figure 2). The  $C_3t$  is in integrated contact with the underlying strata, with a thickness of 50–90 m. It is mainly composed of black-gray mudstone, gray-white medium sandstone, gray coarse sandstone, and coal seam. A layer of bioclastic limestone is locally developed in the lower part, and the bottom is gray-white thick layered medium coarse sandstone and gravelly

coarse sandstone. It is a set of interactive marine coal bearing deposits (Figure 2). The P<sub>1s</sub> is 60–90 m thick. It is mainly composed of gray fine sandstone, black-gray black, sandy mudstone, and coal seam. The bottom of P<sub>1s</sub> is gray-white coarse-grained quartz sandstone. The formation is a set of meandering river and delta plain swamp facies deposits (Figure 2). No. 4 + 5 coal seam in P<sub>1s</sub> and No. 8 + 9 coal seam in C<sub>3t</sub> are continuous and thick. They are the main coal seams in the Baode block and the target seam for CBM development, occurring at a depth of 400–1200 m, with a thickness ranging from 1.16 m to 20.21 m. The lithology of the roof and floor of No. 4 + 5 and No. 8 + 9 coal seams is dominated by mudstone, locally sandy mudstone. The thickness of the roof of the No. 4 + 5 coal seam is 4.3–13.9 m, and the thickness of the floor is 2.4–6.7 m, while those of the 8 + 9 coal seam are 2.8–6.8 m and 2.0–18.6 m, respectively.

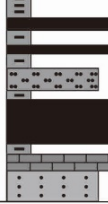
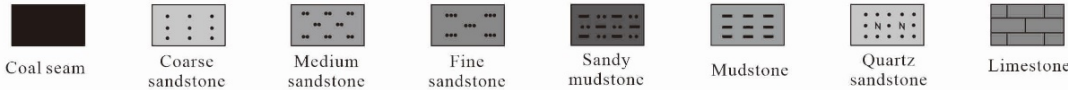
System	Formation	Lithologic section	Thickness (m)	Main coal seam	Lithology description	Sedimentary facies
Permian	Shanxi Formation (P <sub>1s</sub> )		30-116	No. 4+5 coal seam	It is mainly composed of gray fine sandstone, gray black sandy mudstone, and coal seam. The bottom of P <sub>1s</sub> is gray white coarse-grained quartz sandstone.	Meandering river Delta plain
	Taiyuan Formation (P <sub>1t</sub> )		60-90	No. 8+9 coal seam	It is mainly composed of gray mudstone, gray white medium sandstone, gray coarse sandstone, and coal seam. A layer of bioclastic limestone is locally developed in the lower part, and the bottom is gray white thick layered medium coarse sandstone and gravelly coarse sandstone.	Tidal flat Coastal plain river Delta plain
						

Figure 2. Lower Permian stratigraphic column in the Baode block.

### 3. Samples and Analytical Procedures

#### 3.1. Coal and Gas Samples

Eleven coal samples were collected from Wells B1 and B2 (Figure 1c) in the Baode block, and the burial depths of the main coal seams in these two wells are 501.40–547.20 m and 1011.40–1068.30 m, respectively. Among them, four samples were collected from No. 4 + 5 coal seam, and seven of them were collected from No. 8 + 9 coal seam. Part of the sample was carefully packed and then immediately sent to the laboratory for experiments, and another part of the sample was immediately put into different desorption tanks to collect the desorption gas. A total of 54 gas samples were collected from eleven desorption tanks in different desorption periods for gas composition and isotopes analysis.

#### 3.2. Material Composition

Nine of the collected coal samples were analyzed for proximate analysis on an air-dried basis following the Chinese national standard GB/T 212-2008 [18]. According to ISO 7404.3-1994 [19] and ISO 7404.5-1994 [20], mean vitrinite reflectance ( $R_o$ ) measurements and maceral analyses (500 points) were performed on the same polished section of the coal samples using a Leitz MPV-3 photometer microscope. Nonlinear error: max.  $\pm 1$  low significance bit. A/D conversion accuracy:  $\pm 1$  low significance bit, less than 2%.

### 3.3. Pore-Size Distribution

Based on the material composition analysis results, six samples were selected to analyze the characteristic pore-size distributions by using mercury intrusion porosimetry (MIP), low-temperature nitrogen adsorption (LTNA) and X-ray CT. Diameters of pores detected by LTNA range from 2 to 300 nm, and those accessed by MIP are in the diameter of 30–> 1000 nm. Thus, the adsorption pores (<10<sup>2</sup> nm) [21] can be determined by LTNA, while the seepage pores (>10<sup>2</sup> nm) [21] can be well characterized by MIP. MIP was carried out according to the national standard, SY/T 5346-2005 [22], by using Micromeritics Auto Pore IV 9500 instrument. Before the LTNA experiments, all samples were crushed and sieved to a size of 0.18–0.25 mm (60–80 mesh) (dried for 48 h), and then tested using a Micromeritics ASAP2020 instrument at 77K. The X-ray CT was carried out by using U.S. ACTIS-250/320PK/225FFI industrial CT system. The spatial resolution is close to 50 μm in the process of X-ray CT measurement, and therefore large pores and microfractures can be identified in the coal core plug. The specific experimental procedures and image processing methods were presented in detail by Tao et al. (2019) [23].

Thus, the characteristics of seepage pores (>10<sup>2</sup> nm) were measured by MIP, and then the characteristics of adsorption pores (<10<sup>2</sup> nm) were measured by LTNA. Finally, the three-dimensional models of samples' adsorption pores and percolation pores were constructed by X-ray CT experiment.

### 3.4. Gas Composition and Isotopes

A total of 54 gas samples were collected from eleven desorption tanks to analyze the gas composition by using an Agilent 7890B gas chromatograph, according to the Chinese national standard GB/T 13610-2014 [24]. Afterward, δ<sup>13</sup>C values of CH<sub>4</sub> and CO<sub>2</sub>, and δD values of CH<sub>4</sub> of 54 gas samples were determined on a Finnigan MAT 253 mass spectrometer. The δ<sup>13</sup>C and δD values were calibrated with respect to the VPDB and VSMOW standards, and the standard deviations were ±(0.1‰~0.3‰) and ±(1‰~2‰), respectively.

## 4. Results and Discussion

### 4.1. Basic Information of Coals

As shown in Table 1, the Baode coal samples have ash yields ranging from 4.96% to 7.31%, whereas they have relatively high moisture contents (18.6–26.56%) and volatile yields (25.95–30.32%). Higher volatile content means lower coal metamorphism, with R<sub>o</sub> of 0.62–0.76%. The vitrinite content is the highest (41.5–84.8%, mean 69.3%), followed by inertinite (8.7–54.4%, mean 22.8%) and liptinite (0.5–17.0%, mean 7.9%). Macerals in the Baode coal samples include: cutinite, microsporinite, desmocollinite, fusinite, semi-fusinite, resinite, and liptodetrinite. The cutinite is usually distributed in strips, and the microsporinite is distributed in parallel planes in a worm-like shape (Figure 3).

**Table 1.** Results of the proximate and maceral analyses.

Sample No.	Coal Seam No.	Depth (m)	Ro (%)	Maceral Composition (%)			Proximate Analysis (%)		
				Vitrinite	Inertinite	Liptinite	M <sub>ad</sub>	A <sub>ad</sub>	V <sub>ad</sub>
BD-1	4 + 5	501.40–501.70	0.64	74.0	9.0	17.0	22.24	5.33	27.73
BD-2	4 + 5	502.90–503.30	0.67	45.1	54.4	0.5	26.56	4.96	26.46
BD-3	4 + 5	1011.40–1011.70	0.62	83.5	8.7	7.9	24.44	6.55	25.95
BD-4	4 + 5	1011.40–1011.70	0.62	84.8	10.0	5.2	18.60	7.31	30.32
BD-5	8 + 9	546.54–546.84	0.63	76.4	12.7	11.0	26.52	6.44	28.08
BD-6	8 + 9	546.84–547.20	0.68	82.3	14.8	2.8	22.95	7.25	30.12
BD-7	8 + 9	1061.10–1061.40	0.70	81.0	12.9	6.1	22.33	5.30	30.30
BD-8	8 + 9	1065.60–1066.00	0.76	54.7	38.8	6.5	25.73	6.51	30.02
BD-9	8 + 9	1068.00–1068.30	0.75	41.5	44.2	14.4	25.52	6.52	27.25

Notes: M<sub>ad</sub> = moisture content; A<sub>ad</sub> = ash yield; V<sub>ad</sub> = volatile yield; ad = air dried basis.

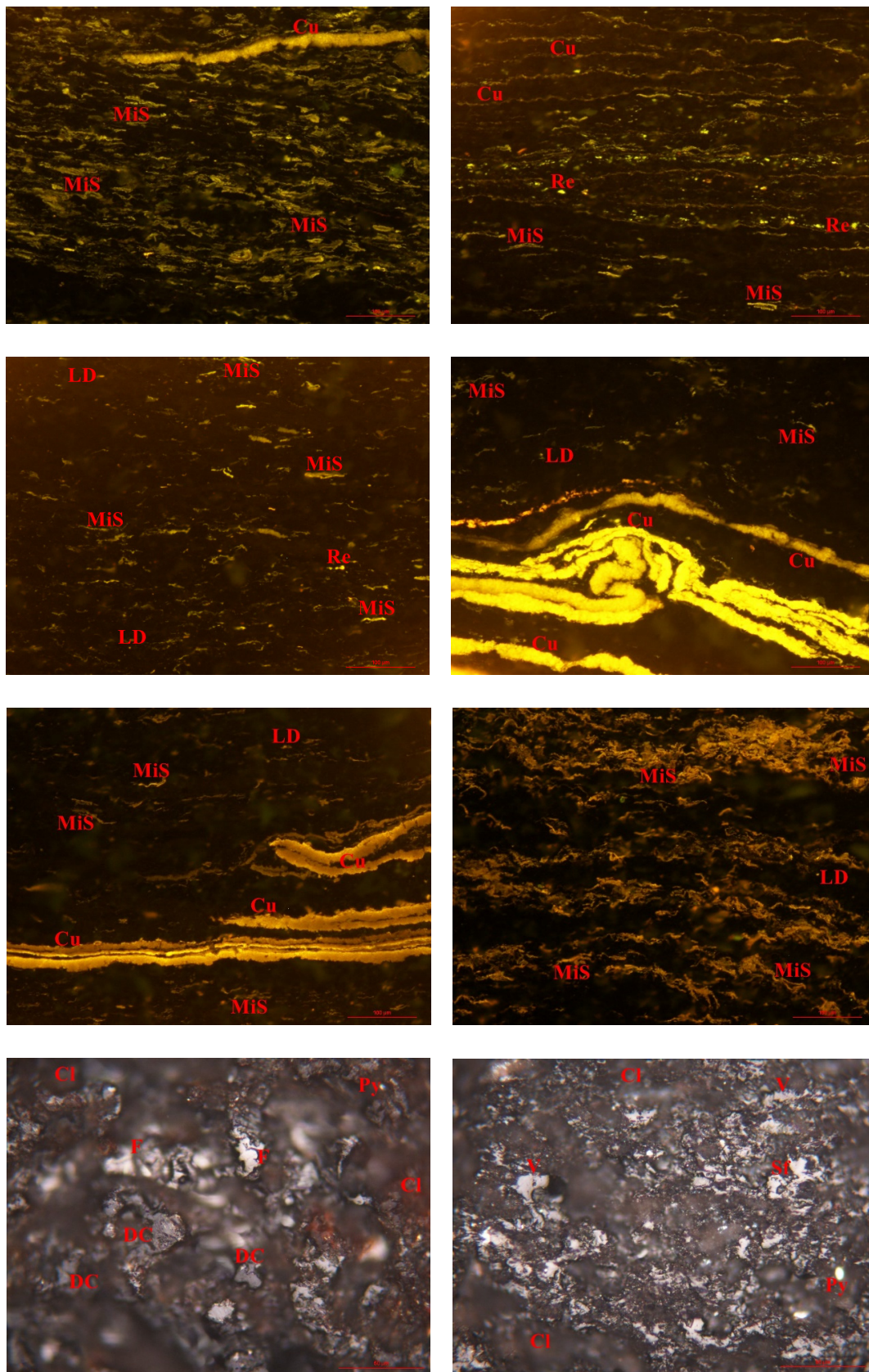


**Figure 3.** Characteristic macerals from Baode coals, polished section, reflected fluorescence and re-  
 flected plane-polarized light (last two pictures). Cu: cutinite; MiS: microsporinite; DC: desmocollinite;  
 F: fusinite; Sf: Semifusinite; Py: Pyrite; V: Vitrinite; Cl: clay; Re: resinite; LD: liptodetrinite.

## 4.2. CBM Composition and Origin

### 4.2.1. Compositional Characteristics of CBM

As shown in Table 2, the gas in No. 4 + 5 and No. 8 + 9 coal seams are dominated by CH<sub>4</sub>, with a volume fraction ranging from 80.9% to 94.7% (mean 88.32%). The volume fraction of N<sub>2</sub> varies between 0.6–15.9% (mean 4.95%), and the N<sub>2</sub> content in No. 4 + 5 coal seam is higher than that in No. 8 + 9 coal seam. Meanwhile, as the depth increases, the N<sub>2</sub> content decreases relatively, which shows that the gas composition of shallow CBM is affected by mixing with atmospheric air [25,26]. Figure 4 indicates that the N<sub>2</sub> volume fraction and CH<sub>4</sub> volume fraction in the two sets of coal seams are negatively correlated. The main difference between 8 + 9 coal seam (a) and 8 + 9 coal seam (b) is the different proportions of N<sub>2</sub> and CH<sub>4</sub>. Different proportions can characterize the source of coal seam gas. The proportion of gas in No. 8 + 9 coal seam (a) is the same as that in No. 4 + 5 coal seam. The CO<sub>2</sub> content increases with increasing burial depth of No. 8 + 9 coal seam. This phenomenon is related to the action of CO<sub>2</sub>-reducing bacteria in the shallow part which decreases with depth [27].

**Table 2.** CBM composition of the collected gas samples from eleven desorption tanks in different desorption periods.

Coal Seam No.	Depth/m	Sample No.	Volume Fraction of Each Component in CBM (%)			Coal Seam No.	Depth/m	Sample No.	Volume Fraction of Each Component in CBM (%)				
			CO <sub>2</sub>	N <sub>2</sub>	CH <sub>4</sub>				CO <sub>2</sub>	N <sub>2</sub>	CH <sub>4</sub>		
4 + 5	501.40–501.70	B1-1	B1-1-1	3.0	10.2	86.7	546.84–547.20	B1-4	B1-4-3	3.3	10.7	86.0	
			B1-1-2	3.6	8.8	87.4			B1-4-4	3.5	9.9	86.6	
			B1-1-3	3.3	7.6	89.1			B1-4-5	3.6	5.6	90.8	
			B1-1-4	3.4	6.0	90.6			B1-4-6	1.9	4.7	93.5	
			B1-1-5	1.6	4.3	94.1			B2-3-1	9.0	2.8	88.1	
	502.90–503.30	B1-2	B1-2-1	3.1	15.9	80.9		1061.10–1061.40	B2-3	B2-3-2	9.4	2.6	87.9
			B1-2-2	3.8	15.2	81.1				B2-3-3	9.0	2.5	88.3
			B1-2-3	3.2	12.7	84.1				B2-3-4	8.6	2.7	88.5
			B1-2-4	3.8	9.4	86.8				B2-3-5	8.9	2.5	88.4
			B1-2-5	2.4	5.7	91.9				B2-4-1	10.6	1.9	87.3
	1011.40–1011.70	B2-1	B2-1-1	3.5	4.5	92.0	1064.00–1064.35	B2-4	B2-4-2	10.4	1.6	87.8	
			B2-1-2	4.1	3.7	92.1			B2-4-3	10.7	1.7	87.4	
			B2-1-3	4.8	3.0	92.2			B2-4-4	12.0	2.1	85.7	
			B2-1-4	3.8	3.0	93.2			B2-4-5	10.2	1.7	88.0	
			B2-1-5	2.2	3.1	94.7			B2-5-1	9.3	1.7	88.7	
	1014.80–1015.20	B2-2	B2-2-1	3.0	8.2	88.6	1065.60–1066.00	B2-5	B2-5-2	9.2	1.6	88.8	
			B2-2-2	3.2	7.7	88.8			B2-5-3	10.7	1.5	87.4	
			B2-2-3	2.4	6.5	90.8			B2-5-4	12.0	1.7	85.8	
			B2-2-4	3.0	5.9	90.7			B2-6-1	9.7	5.5	82.6	
			B2-2-5	3.6	3.3	92.6			B2-6-2	13.1	2.6	82.2	
8 + 9	546.54–546.84	B1-3	B1-3-1	4.3	8.5	87.1	1066.80–1067.10	B2-6	B2-6-3	11.6	1.2	84.9	
			B1-3-2	4.0	4.8	91.2			B2-6-4	11.7	1.1	85.0	
			B1-3-3	4.5	2.6	92.9			B2-6-5	9.7	0.7	87.3	
			B1-3-4	4.4	2.2	93.4			B2-7-1	7.8	1.2	88.0	
			B1-3-5	4.7	2.2	93.2			B2-7-2	9.5	0.6	87.2	
	546.84–547.20	B1-4	B1-4-1	3.1	11.5	85.4	1068.00–1068.30	B2-7	B2-7-3	9.6	2.7	84.1	
			B1-4-2	2.7	14.0	83.3			B2-7-4	6.7	1.6	87.9	

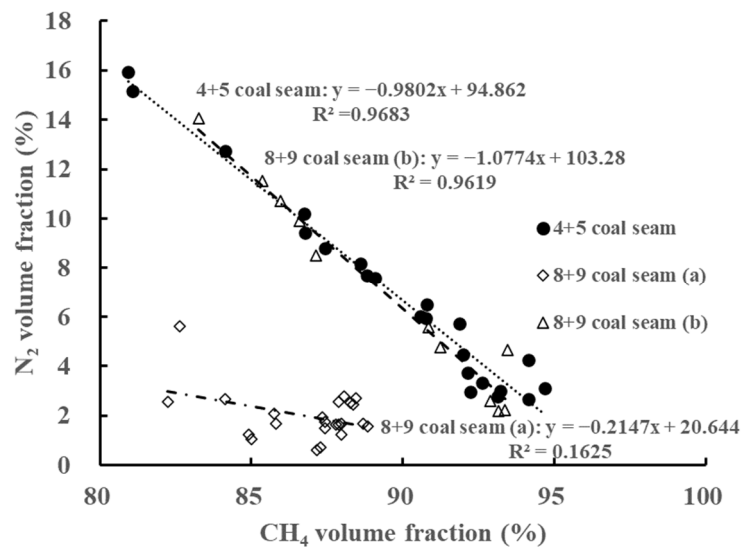


**Figure 4.** Relationship between  $N_2$  volume fraction and  $CH_4$  volume fraction.

#### 4.2.2. Genetic Types of $CH_4$ and $CO_2$

CBM is divided into biogenic gas and thermogenic gas, and the thermogenic gas is further subdivided into early thermogenic wet gas and late thermogenic dry gas [28]. To some extent, different gas concentrations in CBM reflect the genesis of CBM which can be identified by gas composition.

As shown in Table 3, the value of  $\delta^{13}C$  ( $CH_4$ ) in No. 4 + 5 coal seam varies between  $-55.6\text{‰}$  and  $-47.7\text{‰}$ , with an average of  $-52.5\text{‰}$ , and the value of that in No. 8 + 9 coal seam varies between  $-62.3\text{‰}$  and  $-50.4\text{‰}$ , with an average of  $-54.5\text{‰}$ . The  $\delta^{13}C$  ( $CH_4$ ) values of the two coal seams are within the range of national  $\delta^{13}C$  ( $CH_4$ ) observation values of CBM (from  $-73.7\text{‰}$  to  $-24.9\text{‰}$ ) [29], belonging to light carbon isotopes. The value of  $\delta^{13}D$  ( $CH_4$ ) in No. 4 + 5 coal seam ranges from  $-256.2\text{‰}$  to  $-241.6\text{‰}$ , with an average of  $-249.4\text{‰}$ , and the value of that in No. 8 + 9 coal seam ranges from  $-261.8\text{‰}$  to  $-247.6\text{‰}$ , with an average of  $-252.8\text{‰}$ . At shallower than 550 m, the average value of  $\delta^{13}C$  ( $CH_4$ ) is less than  $-55\text{‰}$ , indicating that biogenic gas is the main source. With the increase in burial depth (about 1000 m in Table 3), the average value of  $\delta^{13}C$  ( $CH_4$ ) is around  $-50\text{‰}$ , indicating that thermogenic gas is dominant. Figure 5 also shows that No. 4 + 5 and No. 8 + 9 coal seams both have biogenic gas and thermogenic gas [30].

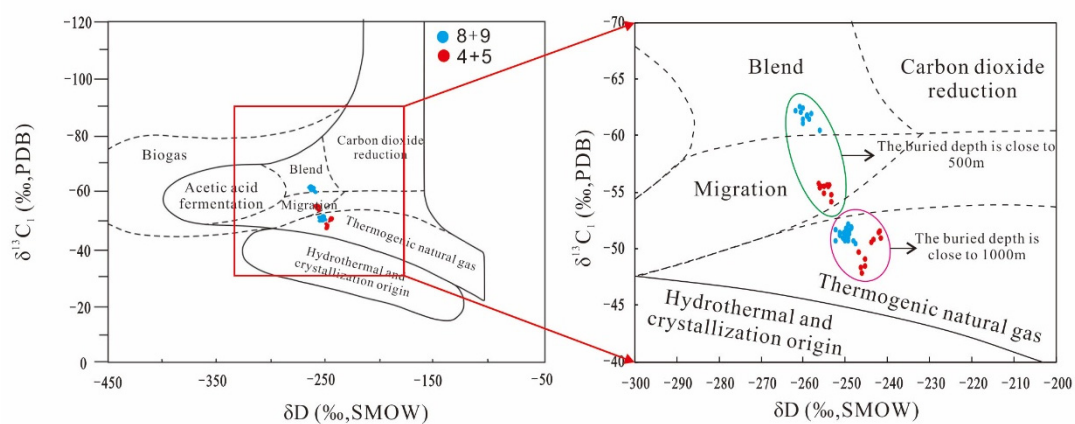


**Figure 5.** Genetic type discrimination map of CBM. ( $C_1$  stands for  $CH_4$ ) (modified from [31]).

**Table 3.** Carbon and hydrogen stable isotope compositions and CDMI values of gas samples from eleven desorption tanks in different desorption periods.

Coal Seam No.	Depth/m	Sample No.	$\delta^{13}\text{C}$ (‰)		$\delta\text{D}$ (‰)	CDMI	Coal Seam No.	Depth/m	Sample No.	$\delta^{13}\text{C}$ (‰)		$\delta\text{D}$ (‰)	CDMI	
			$\text{CH}_4$	$\text{CO}_2$						$\text{CH}_4$	$\text{CO}_2$			
4 + 5	501.40–501.70	B1-1	B1-1-1	−55.5	−7.2	−253.6	3.4	546.84–547.20	B1-4	B1-4-4	−61.5	−9.6	−259.0	3.9
			B1-1-2	−54.6	−7.3	−253.2	3.9			B1-4-5	−61.3	−9.2	−259.9	3.8
			B1-1-3	−55.4	−6.0	−253.9	3.6			B1-4-6	−60.3	−11.3	−256.0	2.0
			B1-1-4	−55.5	−5.6	−254.3	3.6			average	−61.4	−10.5	−259.3	/
			B1-1-5	−54.0	−9.8	−253.2	1.7			1061.10–1061.40	B2-3	B2-3-1	−51.5	3.1
	average	−55	−7.2	−253.7	/	B2-3-2	−51.4	3.4	−248.9			9.6		
	502.90–503.30	B1-2	B1-2-1	−55.6	−10.5	−256.2	3.7	B2-3-3	−51.2			3.7	−250.2	9.3
			B1-2-2	−55.4	−9.2	−255.8	4.4	B2-3-4	−50.8			4.2	−250.6	8.9
			B1-2-3	−55.3	−8.0	−255.1	3.6	B2-3-5	−50.5			3.7	−252.3	9.2
			B1-2-4	−55.3	−6.9	−255.9	4.2	average	−51.1	3.6	−250.9	/		
			B1-2-5	−54.8	−9.0	−254.9	2.6	B2-4-1	−51.7	5.1	−248.5	10.8		
	average	−55.3	−8.7	−255.6	/	1064.00–1064.35	B2-4	B2-4-2	−51.6	5.5	−249.4	10.6		
	1011.40–1011.70	B2-1	B2-1-1	−51.4	−1.8			−241.6	3.7	B2-4-3	−51.7	5.2	−249.7	10.9
			B2-1-2	−51.3	−1.9			−242.1	4.3	B2-4-4	−51.3	6.7	−250.3	12.3
			B2-1-3	−50.9	−0.9			−241.6	5	B2-4-5	−50.5	4.8	−249.2	10.4
			B2-1-4	−50.8	−2.9			−243.1	3.9	average	−51.4	5.4	−249.4	/
			B2-1-5	−50.5	−2.8	−243.8	2.3	B2-5-1	−52.0	1.8	−249.2	9.5		
	average	−51	−2.1	−242.5	/	1065.60–1066.00	B2-5	B2-5-2	−51.4	7.6	−251.2	9.4		
	1014.80–1015.20	B2-2	B2-2-1	−49.6	−6.5			−246.6	3.2	B2-5-3	−51.0	5.5	−251.3	10.9
			B2-2-2	−49.0	−1.0			−245.3	3.5	B2-5-4	−50.5	4.9	−250.0	12.3
B2-2-3			−48.4	−6.6	−245.3			2.6	average	−51.2	5	−250.4	/	
B2-2-4			−48.2	−3.8	−246.1			3.2	B2-6-1	−51.8	2.8	−248.5	10.5	
B2-2-5			−47.7	−0.6	−245.9	3.8	B2-6-2	−51.5	7.1	−249.2	13.7			
average	−48.6	−3.7	−245.9	/	1066.80–1067.10	B2-6	B2-6-3	−51.4	5.6	−249.3	12.0			
546.54–546.84	B1-3	B1-3-1	−61.3	−12.0			−258.4	4.7	B2-6-4	−51.2	5.8	−249.1	12.1	
		B1-3-2	−62.3	−10.3			−259.9	4.2	B2-6-5	−51.1	5.4	−250.0	10	
		B1-3-3	−62.0	−8.8			−261.8	4.6	average	−51.4	5.3	−249.2	/	
		B1-3-4	−61.8	−8.8			−258.0	4.5	B2-7-1	−51.1	5.2	−249.7	8.1	
		B1-3-5	−61.6	−9.0	−258.9	4.8	1068.00–1068.30	B2-7	B2-7-2	−50.4	3.8	−247.6	9.8	
average	−61.8	−9.8	−259.4	/	B2-7-3	−50.9			5.1	−249.2	10.2			
546.84–547.20	B1-4	B1-4-1	−62.3	−12.4	−260.7	3.5			B2-7-4	−50.6	5.8	−248.0	7.1	
		B1-4-2	−61.9	−11.0	−260.5	3.1			average	−50.7	5	−248.6	/	
		B1-4-3	−60.9	−9.6	−259.8	3.7								

$\text{CO}_2$  in CBM is mainly generated in the low maturity evolution stage of organic matter, which is generated through the chemical reaction of oxygen-containing groups such as decarboxylation and carbonyl in coal molecules [31]. Previous studies have shown that the value of  $\delta^{13}\text{C}$  in organic  $\text{CO}_2$  is generally  $-39\text{‰} \sim -8\text{‰}$ , where the value of  $\delta^{13}\text{C}$  ( $\text{CO}_2$ ) produced by humic organic matter is generally  $-25\text{‰} \sim -5\text{‰}$ ; while the value of  $\delta^{13}\text{C}$  ( $\text{CO}_2$ ) produced by thermal degradation of organic matter is  $-28\text{‰} \sim -10\text{‰}$ , and the value of  $\delta^{13}\text{C}$  ( $\text{CO}_2$ ) transformed by microbial reduction is more important, reaching  $18\text{‰}$ . In the study area, the  $\delta^{13}\text{C}$  ( $\text{CO}_2$ ) value in No. 4 + 5 coal seam is between  $-10.5\text{‰}$  and  $-0.6\text{‰}$ , and that in No. 8 + 9 coal seam is between  $-11.3\text{‰}$  and  $-7.6\text{‰}$  (Table 3), which conforms to the carbon isotope characteristics of organic (biological) genetic gas. Among them, some samples have higher  $\delta^{13}\text{C}$  ( $\text{CO}_2$ ) values due to microbial transformation. The burial depth also affects the  $\delta^{13}\text{C}$  ( $\text{CO}_2$ ) values. The burial depth of No. 4 + 5 coal seam and No. 8 + 9 coal seam in the same well is similar, but that of the same coal seam in different wells (such as No. 4 + 5 coal seam in wells B1 and B2) is quite different. Therefore, the  $\delta^{13}\text{C}$  ( $\text{CO}_2$ ) values of samples are separated in two groups in Figure 5.

According to the component data of CBM, the CO<sub>2</sub>–CH<sub>4</sub> coefficient of each sample is calculated by:

$$\text{CDMI} = \frac{\text{CO}_2}{\text{CO}_2 + \text{CH}_4} \times 100\%$$

The CDMI value and the  $\delta^{13}\text{C}$  (CO<sub>2</sub>) are used to draw the relationship diagram reflecting the genetic types of CO<sub>2</sub> (Figure 6). No. 4 + 5 and No. 8 + 9 coal seams both contain CO<sub>2</sub> generated by coal pyrolysis, which belongs to organic genetic gas [28], while shallow CO<sub>2</sub> is greatly affected by the action of microorganisms and belongs to biogenic gas. In the stagnant CBM system, the water-soluble consumption of CO<sub>2</sub> produced by coalification (including associated gas during microbial methane production and thermal degradation gas of coal-forming material) is not complete [32], resulting in high CO<sub>2</sub> concentration in gas components, and increases with the increase of burial depth.

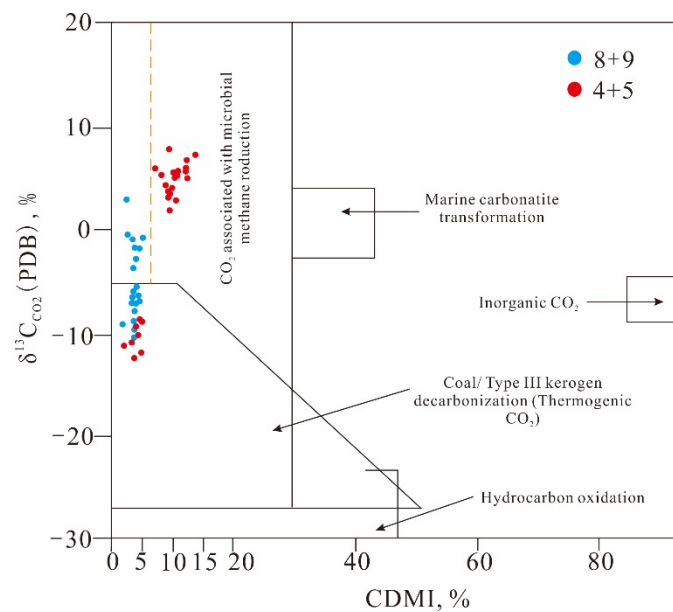


**Figure 6.** Relationship between  $\delta^{13}\text{C}$  (CO<sub>2</sub>) and CDMI.

#### 4.3. Characterization of Gas Storage and Seepage Space

##### 4.3.1. Characteristics of Seepage Pores

The experimental data of mercury injection are shown in Table 4, and the mercury injection curves are shown in Figure 7. The pores contained in the coal samples are mainly micropores and transition pores, and the development of mesopores and macropores is less. The average proportion of pores in each pore size class is 56.61%, 28.22%, 5.10%, and 10.07%, respectively. Mercury injection curves can be divided into three types. Type 1 contains samples BD-1 and BD-3. At pressures lower than 10 MPa, the amount of mercury injected increased rapidly; at pressures greater than 10 MPa, the amount of mercury injected increased slowly, indicating that micropores are more developed. The mercury intrusion curve and the extrusion curve basically overlap, indicating that the mercury removal efficiency is high and the pore connectivity is good. Type 2 contains BD-5 and BD-6. At pressures below 10 MPa, the amount of mercury injected increased slowly, and at pressures greater than 10 MPa, the amount of mercury increased rapidly, indicating that the pore structure is dominated by micropores. The large offset between the mercury injection curve and the mercury extrusion curve shows the low mercury removal efficiency and poor pore connectivity. The Type 3 mercury injection curve of BD-2 and BD-9 has a three-stage structure. At pressures less than 2 MPa, the mercury injection curve rises linearly; at pressures between 2 MPa and 10 MPa, the mercury injection rate gradually slows down; at pressures greater than 10 MPa, the mercury injection rate increases again, indicating

that compared with the first two types of curves, mesopores and macropores are more developed in samples BD-2 and BD-9.

**Table 4.** Mercury injection data of typical samples in the Baode block.

Sample No.	Coal Seam No.	Porosity (%)	Pore Volume Percentage (%)			
			Micropore (<10 nm)	Transition Pores (10–10 <sup>2</sup> nm)	Mesopore (10 <sup>2</sup> –10 <sup>3</sup> nm)	Macropore (>10 <sup>3</sup> nm)
BD-1	4 + 5	5.07	64.09	26.41	2.46	7.04
BD-2	4 + 5	5.39	61.15	22.19	3.99	12.67
BD-3	8 + 9	5.42	62.24	26.58	3.35	7.83
BD-5	8 + 9	6.89	54.89	31.38	4.65	9.08
BD-6	8 + 9	6.09	47.91	32.87	9.61	9.60
BD-9	8 + 9	5.29	49.38	29.89	6.54	14.19

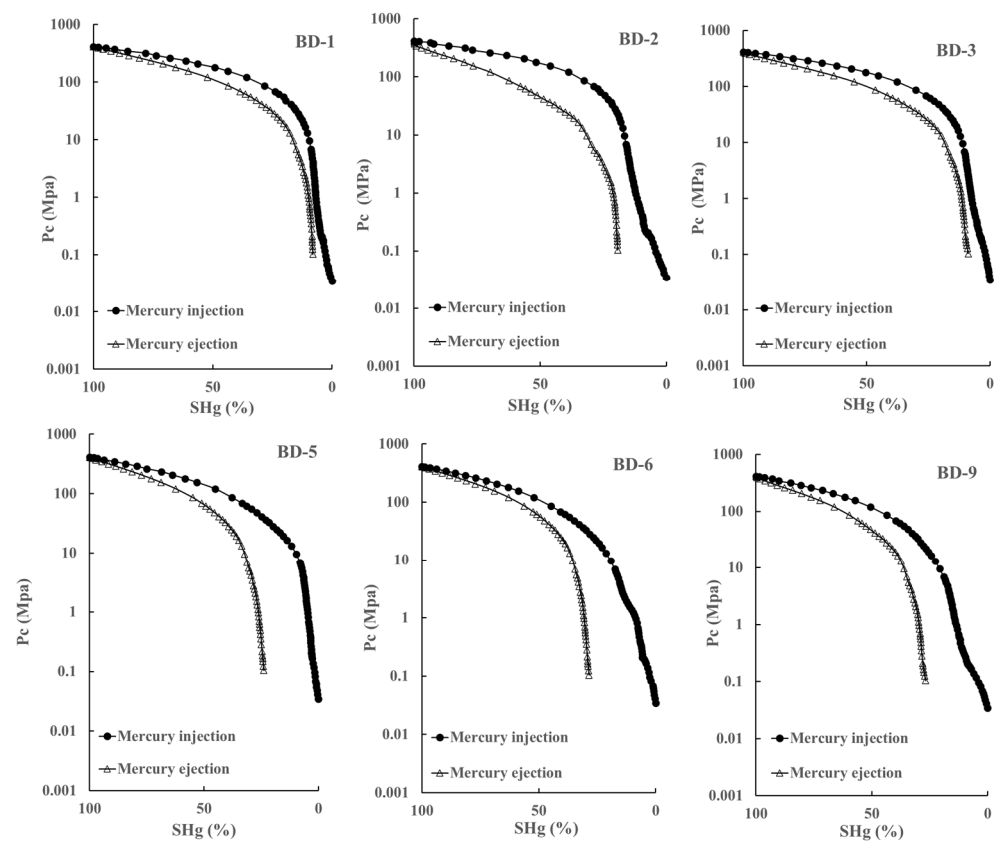


**Figure 7.** Mercury injection curves of typical samples in the study area.

Overall, the seepage pores (>10<sup>2</sup> nm) are poorly developed in Baode coal samples. Compared with No. 4 + 5 coal samples, No. 8 + 9 coal samples have a relatively small hysteresis and good pore connectivity. At the same time, the proportion of mesopores and macropores is relatively high, which is conducive to gas migration (Table 4).

#### 4.3.2. Characteristics of Adsorption Pores

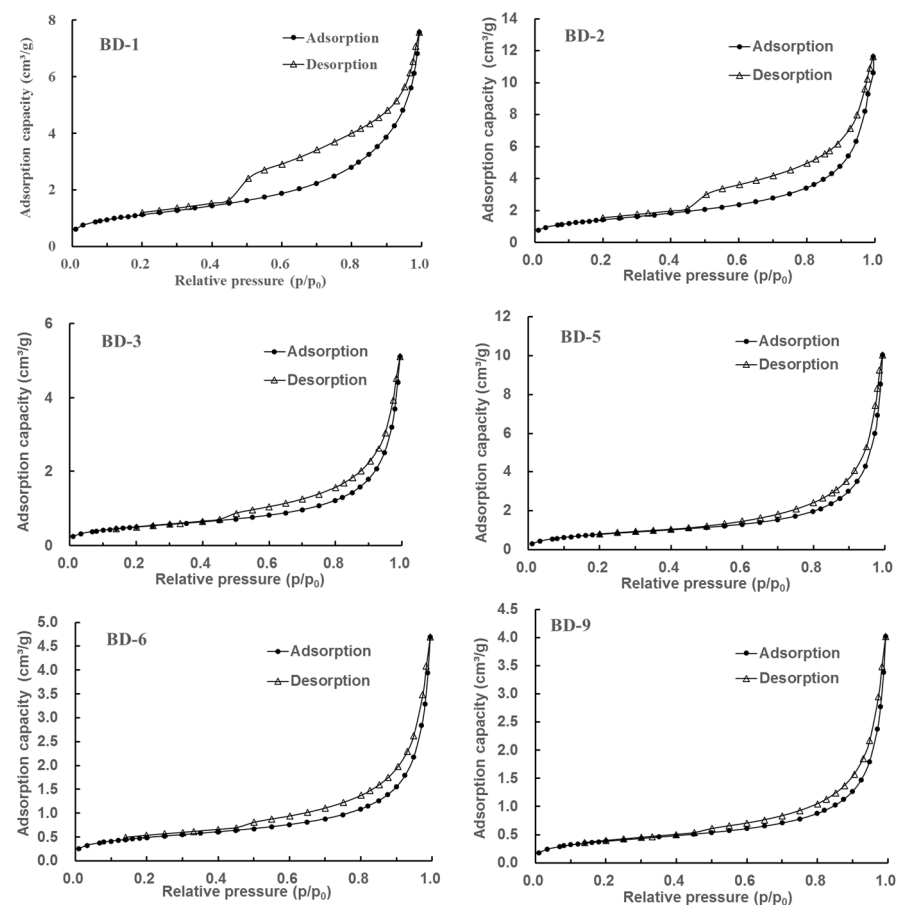
Low-temperature liquid nitrogen adsorption experiments are often used to finely characterize the adsorption pores (<10<sup>2</sup> nm) of coal samples [33,34]. As shown in Table 5, the BET specific surface area (SSA) is 1.41–5.14 m<sup>2</sup>/g, and the total pore volume of BJH is 0.0063–0.0166 mL/g. The average pore diameter (APD) ranges from 11.50 nm to 19.86 nm, and the proportion of transition pores is the largest.

**Table 5.** Nitrogen adsorption data of typical samples in the study area.

Sample No.	Coal Seam No.	BET SSA (m <sup>2</sup> /g)	BJH TPV (10 <sup>-3</sup> mL/g)	APD (nm)	Pore Volume Percentage (%)		
					<10 nm	10–100 nm	>100 nm
BD-1	4 + 5	4.04	0.0119	11.50	29.55	50.33	20.12
BD-2	4 + 5	5.14	0.0166	12.51	24.12	62.65	13.23
BD-3	8 + 9	1.81	0.0080	17.17	16.31	55.01	28.68
BD-5	8 + 9	2.93	0.0156	19.86	12.76	55.12	32.12
BD-6	8 + 9	1.76	0.0074	17.73	16.20	52.69	31.11
BD-9	8 + 9	1.41	0.0063	18.33	14.34	52.41	33.25

Notes: BJH TPV = Total pore volume; APD = Average pore diameter; BET SSA = Specific surface area.

Based on the adsorption/desorption curve of the nitrogen adsorption experiment, scholars use the hysteresis loop to classify the pore morphology in coal [35–37]. As can be seen in Figure 8, the pore morphology of the samples is divided into two types. Type 1 contains samples of BD-1 and BD-2 collected from No. 4 + 5 coal samples, which has an obvious hysteresis loop located at the relative pressure of 0.5–1, indicating that ink bottle pores are well-developed in No. 4 + 5 coal samples. Type 2 contains samples BD-3, BD-5, BD-6, and BD-9, which belong to the No. 8 + 9 coal samples. There is no hysteresis loop or an obvious hysteresis loop, which means that the inflection point of desorption curve is not obvious, thus the adsorption and desorption curves are roughly parallel, indicating that the samples mainly develop an airtight pore closed at one end.

**Figure 8.** Typical nitrogen adsorption and desorption curve of coal samples in Baode block.

As shown in Figure 9, all samples have pores with a diameter of 1–100 nm, and micropores with a pore diameter of less than 10 nm are less developed, and there is a peak around 40–50 nm. The contribution of SSA is dominated by 1–10 nm micropores. The

difference is that the 1–3 nm pores of the No. 4 + 5 coal samples have a great contribution, while the 3–10 nm pores of the No. 8 + 9 coal samples have a great contribution. Compared with No. 8 + 9 coal samples, No. 4 + 5 coal samples have developed more adsorbed pores such as ink bottle pores, so the SSA is relatively large, which is conducive to the adsorption of CBM but not conducive to desorption.

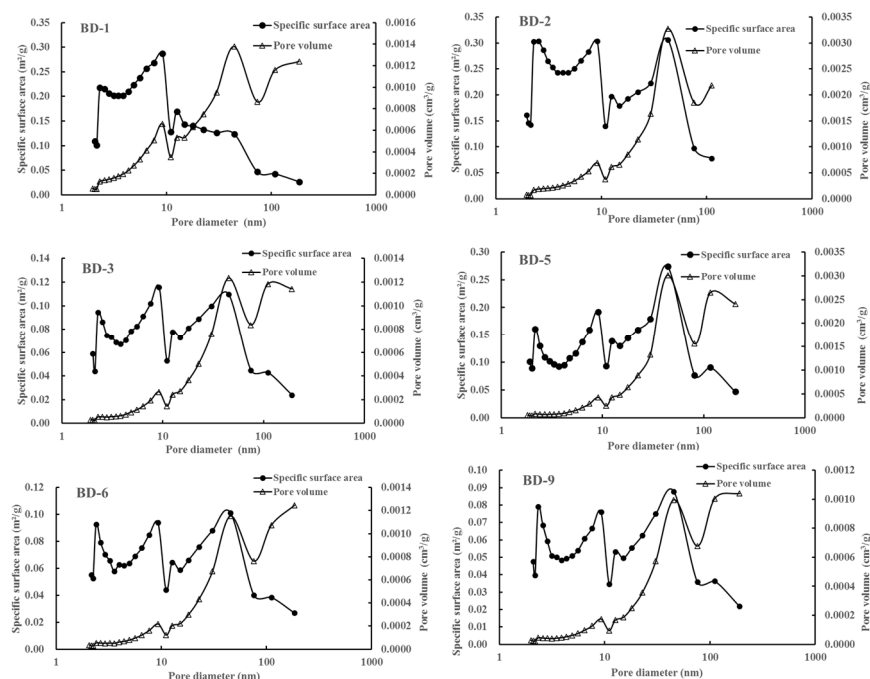


**Figure 9.** Relationship between pore diameter, SSA, and pore volume of typical coal samples in Baode block.

The BET model, FHH model, and thermodynamic model are often used to calculate the fractal dimension of micropores of coal [38,39]. In this paper, the FHH model is used to calculate the fractal dimension based on nitrogen adsorption data;

$$\ln(V/V_0) = A \ln(\ln P/P_0) + C$$

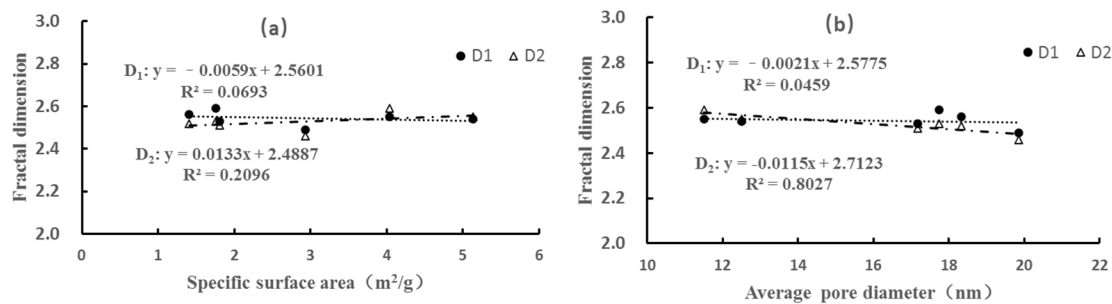
where  $V$  is the volume of gas molecules adsorbed at equilibrium pressure;  $V_0$  is the volume of gas adsorbed by the monolayer;  $P_0$  is the saturated vapor pressure of gas adsorption;  $A$  is the slope of the double logarithm curve of  $\ln V$  and  $\ln(\ln(P_0/P))$ ;  $C$  is a constant.

In the process of liquid nitrogen adsorption, micropores are filled first, and then monolayer adsorption occurs, followed by multi-molecular layer adsorption. When the relationship between the relative pressure and pore diameter conforms to the Kelvin equation, capillary condensation occurs [40]. Therefore, taking the relative pressure as the boundary of 0.5 [40], the fractal dimensions  $D_1$  and  $D_2$  can be calculated respectively (Table 6). The fractal dimension  $D$  should meet  $2 \leq D \leq 3$ , in which the larger the fractal dimension, the rougher the coal surface and the stronger the adsorption capacity [41,42].

**Table 6.** Fractal dimension of typical samples in the study area.

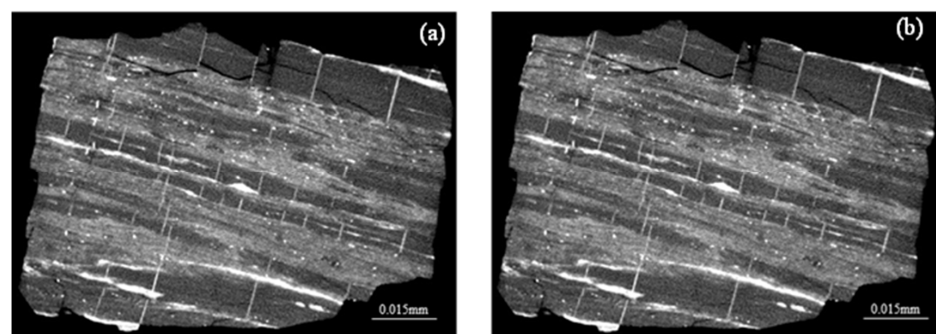
Sample No.	Relative Pressure (P/P <sub>0</sub> ): 0~0.5			Relative Pressure (P/P <sub>0</sub> ): 0.5~1		
	A <sub>1</sub>	D <sub>1</sub> = 3 + A <sub>1</sub>	R <sub>1</sub> <sup>2</sup>	A <sub>2</sub>	D <sub>2</sub> = 3 + A <sub>2</sub>	R <sub>2</sub> <sup>2</sup>
BD-1	−0.45	2.55	0.9997	−0.41	2.59	0.9864
BD-2	−0.46	2.54	0.9996	−0.45	2.55	0.9996
BD-3	−0.47	2.53	0.9975	−0.49	2.51	0.9996
BD-5	−0.51	2.49	0.9908	−0.54	2.46	0.9991
BD-6	−0.41	2.59	0.9962	−0.47	2.53	0.9999
BD-9	−0.44	2.56	0.9947	−0.48	2.52	0.9987

As shown in Figure 10, the fractal dimension  $D_1$  has no obvious correlation with the SSA and APD. The fractal dimension  $D_1$  reflects the porosity of the sample with a relative pressure of 0~0.5, which cannot characterize all the pore characteristics of the sample. The fractal dimension  $D_2$  is positively correlated with the SSA and negatively correlated with the APD, which indicates that the larger the SSA, the smaller the average pore size, and the higher the overall micropore proportion of the sample. It indicates that the more developed the micropore, the stronger the adsorption capacity of coal. As the value of  $D_2$  increases, the pore structure becomes more complex, and the adsorption capacity of coal becomes stronger.

**Figure 10.** (a) Relationship between fractal dimension and SSA; (b) Relationship between fractal dimension and APD.

#### 4.3.3. Three-Dimensional Model of Storage and Seepage Space

In order to intuitively obtain the distribution characteristics of pores and fractures, the samples are selected for X-ray CT imaging tests (Table 7). The results show that the porosity of the selected coal samples varies from 0.76% to 4.39%, with an average of 2.38%. However, the proportion of connected pores is extremely low (0–35.04%), resulting in an extremely low connected porosity of 0–1.21%. There is a negative correlation between the porosity and the mineral content. Sample BD-3 has the lowest porosity, because most of the fractures inside the sample are filled with minerals (Figure 11).

**Figure 11.** Two-dimensional slices of mineral filling fractures in sample BD-3 ((a) is the first slice and (b) is the 45th slice; white means the fractures are filled with minerals).

**Table 7.** X-ray CT imaging test results of typical samples.

Sample No.	Porosity (%)	Connected Porosity (%)	Proportion of Connected Pores (%)	Mineral Content (%)
BD-1	1.97	0	0	3.31
BD-2	3.92	0.79	20.15	0.27
BD-3	0.76	0.07	9.21	4.5
BD-5	4.39	1.21	27.56	0.26
BD-6	1.17	0.41	35.04	3.52
BD-9	3.47	0.17	4.85	2.17

After three-dimensional reconstruction, the distribution of the coal matrix, pores, fractures, and minerals in coal samples can be more easily displayed (Figure 12). The distribution direction of minerals is similar to the direction of densely developed pores, especially in samples BD-3 and BD-6, and the distribution of pores and fractures is extremely uneven. Meanwhile, although some samples have relatively high porosity, such as BD-9, due to the extremely low proportion of connected pores, the connected porosity is still very low. On the contrary, if the mineral content in coal is small and distributed in a dispersed state, the proportion of connected pores will be high, and the connected porosity will be high, which is conducive to gas flow, such as sample BD-5. Therefore, it is not the measured porosity that plays a key role in the development of CBM, but it depends on the connectivity of the pore and fracture system.

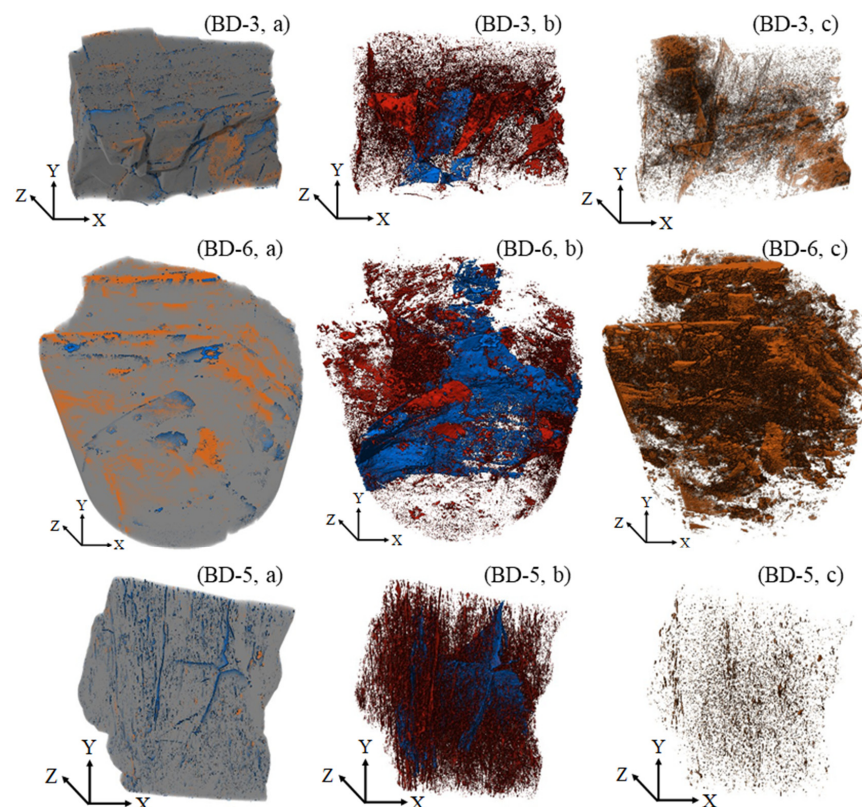


**Figure 12.** (a) Three-dimensional reconstruction image of coal samples (gray: matrix, blue: pores and fractures, orange: mineral). (b) Three-dimensional image of connected and isolated pores and fractures (blue: connected pores and fractures, red: isolated pores and fractures). (c) Three-dimensional image of minerals.

## 5. Conclusions

(1) Gases disrobed from No. 4 + 5 and No. 8 + 9 coal seams in Baode block are dominated by CH<sub>4</sub>, followed by N<sub>2</sub> and CO<sub>2</sub>. Under the influence of air mixing, the N<sub>2</sub> content decreases with the increase of burial depth. Meanwhile, the CO<sub>2</sub> content increases with increasing burial depth of No. 8 + 9 coal seam, which related to the action of CO<sub>2</sub>-reducing bacteria in the shallow part.

(2) The δ<sup>13</sup>C (CO<sub>2</sub>) value in No. 4 + 5 coal seam is between −10.5‰ and −0.6‰, and that in No. 8 + 9 coal seam is between −11.3‰ and −7.6‰. No. 4 + 5 and No. 8 + 9 coal seams both have biogenic gas and thermogenic methane. Meanwhile, No. 4 + 5 and No. 8 + 9 coal seams both contain CO<sub>2</sub> generated by thermal maturation of coal (thermogenic gas), while shallow CO<sub>2</sub> is likely to result from the action of microorganisms (microbial gas). With the increase of burial depth, the content of CO<sub>2</sub> increases.

(3) The seepage pores (>10<sup>2</sup> nm) are poorly developed in the Baode coal samples. Samples collected from No. 4 + 5 coal seams have developed more sorption pores such as ink bottle pores, so the SSA is relatively large, which is conducive to the adsorption of CBM. The mercury intrusion and extrusion curves of samples from No. 8 + 9 coal seams exhibit a relatively low degree of hysteresis (Hg retention), indicating good pore connectivity. At the same time, the proportion of mesopores and macropores is relatively high, which is conducive to gas migration.

(4) The porosity of the coal samples is inversely related to the mineral content and the occurrence of the mineral. If the mineral content in coal is small and distributed in a dispersed state, the proportion of connected pores will be high, and the connected porosity will be high, which is conducive to gas flow.

**Author Contributions:** Conceptualization, H.C. and W.T.; methodology, H.C.; software, Z.C.; validation, H.C., W.T. and Q.Z.; formal analysis, S.T.; investigation, S.T.; resources, W.T.; data curation, W.T.; writing—original draft preparation, H.C.; writing—review and editing, W.T.; visualization, Z.C.; supervision, Q.Z.; project administration, H.C.; funding acquisition, W.T. All authors have read and agreed to the published version of the manuscript.

**Funding:** This research was funded by [the National Natural Science Foundation Project] grant number [No. 41772132, 41502157, 41530314], [the Key Project of the National Science & Technology] grant number [No. 2016ZX05043-001], [the Fundamental Research Funds for the Central Universities] grant number [No. 2652019095] and The APC was funded by [the National Natural Science Foundation Project]. Key Technologies R&D Programme of PetroChina Company Limited (2019E-25).

**Institutional Review Board Statement:** Not applicable.

**Informed Consent Statement:** Not applicable.

**Data Availability Statement:** Not applicable.

**Conflicts of Interest:** The authors declare no conflict of interest.

## References

1. Tao, S.; Chen, S.D.; Pan, Z.J. Current status, challenges, and policy suggestions for coalbed methane industry development in China: A review. *Energy Sci. Eng.* **2019**, *7*, 1059–1074. [[CrossRef](#)]
2. Tao, S.; Pan, Z.J.; Tang, S.L.; Chen, S.D. Current status and geological conditions for the applicability of CBM drilling technologies in China: A review. *Int. J. Coal Geol.* **2019**, *202*, 95–108. [[CrossRef](#)]
3. Qin, Y.; Moore, T.A.; Shen, J.; Yang, Z.B.; Shen, Y.L.; Wang, G. Resources and geology of coalbed methane in China: A review. *Int. Geol. Rev.* **2017**, *1*, 777–812.
4. Shao, L.Y.; Wang, X.T.; Wang, D.D.; Li, M.P.; Wang, S.; Li, Y.J.; Shao, K.; Zhang, C.; Gao, C.X.; Dong, D.X.; et al. Sequence stratigraphy, paleogeography, and coal accumulation regularity of major coal-accumulating periods in China. *Int. J. Coal Sci. Technol.* **2020**, *7*, 240–262. [[CrossRef](#)]
5. Chen, Y.; Ma, D.M.; Xia, Y.C.; Guo, C.; Yang, F.; Shao, K. Characteristics of the mud shale reservoirs in coal-bearing strata and resources evaluation in the eastern margin of the Ordos Basin, China. *Energy Explor. Exploit.* **2020**, *38*, 372–405. [[CrossRef](#)]
6. Tao, S.; Tang, D.Z.; Xu, H.; Li, S.; Geng, Y.G.; Zhao, J.L.; Wu, S.; Meng, Q.; Kou, X.; Yang, S.Y.; et al. Fluid velocity sensitivity of coal reservoir and its effect on coalbed methane well productivity: A case of Baode Block, northeastern Ordos Basin, China. *J. Petrol. Sci. Eng.* **2017**, *152*, 229–237. [[CrossRef](#)]

7. Yang, X.C.; Mao, J.S.; Lin, W.J.; Hao, S.; Zhao, L.M.; Wang, Y.; Li, L. Exploration history and enlightenment of coalbed methane in baode block. *Xinjiang Petrol. Geol.* **2021**, *42*, 381–388.
8. Tian, W.G.; Tang, D.Z.; Wang, Z.L.; Sun, B. Origin of coalbed methane in Baode, Northeastern Ordos Basin. *Geol. J. China Univ.* **2012**, *18*, 479–484.
9. Guo, H.G.; Yu, Z.S.; Zhang, H.X. Phylogenetic diversity of microbial communities associated with coalbed methane gas from Eastern Ordos Basin, China. *Int. J. Coal Geol.* **2015**, *150*, 120–126. [[CrossRef](#)]
10. Liu, S.M.; Tan, F.R.; Huo, T.; Tang, S.H.; Zhao, W.X.; Chao, H.D. Origin of the hydrate bound gases in the Juhugeng Sag, Muli Basin, Tibetan Plateau. *Int. J. Coal Sci. Technol.* **2020**, *7*, 43–57. [[CrossRef](#)]
11. Xu, H.; Tang, D.; Liu, D.; Tang, S.; Yang, F.; Chen, X.; Deng, C. Study on coalbed methane accumulation characteristics and favorable areas in the Binchang area, southwestern Ordos Basin, China. *Int. J. Coal Geol.* **2012**, *95*, 1–11. [[CrossRef](#)]
12. Yang, C.; Zhang, J.; Tang, X. Microscopic pore types and its impact on the storage and permeability of continental shale gas, Ordos Basin. *Earth Sci. Front.* **2013**, *20*, 240–250.
13. Xue, G.; Liu, H.; Li, W. Deformed coal types and pore characteristics in Hancheng coalmines in Eastern Weibei coalfields. *Int. J. Min. Sci. Technol.* **2012**, *22*, 681–686. [[CrossRef](#)]
14. Tang, X.; Zhang, J.; Shan, Y.; Xiong, J. Upper Paleozoic coal measures and unconventional natural gas systems of the Ordos Basin, China. *Geosci. Front.* **2012**, *3*, 863–873. [[CrossRef](#)]
15. Wang, L.; Jiang, B.; Qu, Z. Structural control on gas content distribution in eastern margin of Ordos basin. *Coal Geol. Explor.* **2013**, *41*, 14–19.
16. Jiang, B.; Xu, J.; Zhu, K.; Wang, J.; Wang, J.; Qu, Z. Structural and hydrogeological controls of coalbed methane preservation in the eastern Ordos Basin. *Geol. J. China Univ.* **2012**, *3*, 438–446.
17. Cao, D.Y.; Wang, A.M.; Ning, S.Z.; Li, H.T.; Guo, A.J.; Chen, L.M.; Liu, K.; Tan, J.Q.; Zheng, Z.H. Coalfield structure and structural controls on coal in China. *Int. J. Coal Sci. Technol.* **2020**, *7*, 220–239. [[CrossRef](#)]
18. GB/T 212-2008. *Chinese National Standard: Proximate Analysis of Coal*; General Administration of Quality Supervision, Inspection and Quarantine: Beijing, China, 2008. (In Chinese)
19. ISO 7404.3-1994. *Methods for the Petrographic Analysis of Bituminous Coal and Anthracite—Part 3: Method Of Determining Maceral Group Composition*; International Organization for Standardization: Geneva, Switzerland, 1994.
20. ISO 7404.5-1994. *Method for the Petrographic Analysis of bituminous Coal and Anthracite—Part 5: Method of Determining Microscopically the Reflectance of Vitrinite*; International Organization for Standardization: Geneva, Switzerland, 1994.
21. Tao, S.; Zhao, X.; Tang, D.Z.; Deng, C.M.; Meng, Q.; Cui, Y. A model for characterizing the continuous distribution of gas storing space in low-rank coals. *Fuel* **2018**, *233*, 552–557. [[CrossRef](#)]
22. SY/T 5346-2005. *Chinese Petroleum and Natural Gas Industry Standard: Rock Capillary Pressure Measurement*; National Energy Administration: Beijing, China, 2005. (In Chinese)
23. Tao, S.; Pan, Z.J.; Chen, S.D.; Tang, S.L. Coal seam porosity and fracture heterogeneity of marcolithotypes in the Fanzhuang Block, southern Qinshui Basin, China. *J. Nat. Gas Sci. Eng.* **2019**, *66*, 148–158. [[CrossRef](#)]
24. GB/T 13610-2014. *Composition Analysis of Natural Gas by Gas Chromatography*; Standardization Administration of the People's Republic of China: Beijing, China, 2014. (In Chinese)
25. Yang, Z.; Grace, J.R.; Lim, C.J.; Zhang, L. Combustion of low-concentration coal bed methane in a fluidized bed. *Energy Fuels* **2011**, *25*, 975–980. [[CrossRef](#)]
26. Wang, Q.; Dong, S.; Wang, H.; Yang, J.; Huang, H.; Dong, X.; Yu, B. Hydrogeochemical processes and groundwater quality assessment for different aquifers in the Caojiantan coal mine of Ordos Basin, northwestern China. *Environ. Earth Sci.* **2020**, *79*, 199. [[CrossRef](#)]
27. Li, Z.W.; Tang, D.Z.; Tang, S.L.; Pu, Y.F.; Zhang, A.B. Study on formation mechanism of CO<sub>2</sub>-enriched CBM reservoirs in low-rank coal seams from southern Zhunggar Basin. *Coal Sci. Technol.* **2021**, *49*, 174–180.
28. Scott, A.R.; Kaiser, W.R.; Walter, B.; Ayers, J. Thermogenic and secondary biogenic gases, San Juan Basin, Colorado and New Mexico; implications for coalbed gas producibility. *AAPG Bull.* **1994**, *78*, 1186–1209.
29. Qi, Y.; Jiao, S.; Tang, Y.; Ye, J. Characteristics and origins of stable carbon isotope in coalbed methane of China. *J. China Univ. Min. Technol.* **2000**, *29*, 10–17.
30. Whiticar, M.J. Carbon and hydrogen isotope systematics of bacterial formation and oxidation of methane. *Chem. Geol.* **1999**, *161*, 291–314. [[CrossRef](#)]
31. Xu, T.; Xie, Q.; Kang, Y. Heat effect of the oxygen-containing functional groups in coal during spontaneous combustion processes. *Adv. Powder Technol.* **2017**, *28*, 1841–1848. [[CrossRef](#)]
32. Gao, C.; Liu, D.; Li, Z.; Cai, Y.; Fang, Y. Fluid performance in coal reservoirs: A comprehensive review. *Geofluids* **2021**, *2021*, 6611075. [[CrossRef](#)]
33. Tao, S.; Chen, S.D.; Tang, D.Z.; Zhao, X.; Xu, H.; Li, S. Material composition, pore structure and adsorption capacity of low-rank coals around the first coalification jump: A case of eastern Junggar Basin, China. *Fuel* **2018**, *211*, 804–815. [[CrossRef](#)]
34. Men, X.Y.; Tao, S.; Liu, Z.X.; Tian, W.G.; Chen, S.D. Experimental study on gas mass transfer process in a heterogeneous coal reservoir. *Fuel Process. Technol.* **2021**, *216*, 106779. [[CrossRef](#)]

35. Chen, S.D.; Tang, D.Z.; Tao, S.; Chen, Z.L.; Xu, H.; Li, S. Coal reservoir heterogeneity in multi-coal seams of the Panguan syncline, Western Guizhou, China: Implication for the development of superposed CBM-bearing systems. *Energy Fuels* **2018**, *32*, 8241–8253. [[CrossRef](#)]
36. Chen, S.D.; Tang, D.Z.; Tao, S.; Xu, H.; Li, S.; Zhao, J.L.; Jiang, Q.; Yang, H.X. Pore structure characterization of different rank coals using N<sub>2</sub> and CO<sub>2</sub> adsorption and its effect on CH<sub>4</sub> adsorption capacity: A case in Panguan syncline, western Guizhou, China. *Energy Fuels* **2017**, *31*, 6034–6044. [[CrossRef](#)]
37. Wang, C.; Hao, S.; Sun, W.; Chu, W. Fractal dimension of coal particles and their CH<sub>4</sub> adsorption. *Int. J. Coal Sci. Technol.* **2012**, *22*, 855–858.
38. Kim, D.; Seo, Y.; Kim, J.; Han, J.; Lee, Y. Experimental and simulation studies on adsorption and diffusion characteristics of coalbed methane. *Energies* **2019**, *12*, 3445. [[CrossRef](#)]
39. Friesen, W.I.; Mikula, R.J. Fractal dimensions of coal particles. *J. Colloid Interface Sci.* **1987**, *120*, 263–271. [[CrossRef](#)]
40. Zelenka, T. Adsorption and desorption of nitrogen at 77 K on micro- and mesoporous materials: Study of transport kinetics. *Micropor. Mesopor. Mater.* **2016**, *227*, 202–209. [[CrossRef](#)]
41. Chen, S.D.; Tang, D.Z.; Tao, S.; Ji, X.Y.; Xu, H. Fractal analysis of the dynamic variation in pore-fracture systems under the action of stress using a low-field NMR relaxation method: An experimental study of coals from western Guizhou in China. *J. Petrol. Sci. Eng.* **2019**, *173*, 617–629. [[CrossRef](#)]
42. Chen, Y.; Tang, D.Z.; Xu, H.; Tao, S.; Li, S.; Yang, G.H.; Yu, J.J. Pore and fracture characteristics of different rank coals in the eastern margin of the Ordos Basin, China. *J. Nat. Gas Sci. Eng.* **2015**, *26*, 1264–1277. [[CrossRef](#)]